A SPICE model of Operational Amplifiers for Electromagnetic Compatibility Analysis

A SPICE Model of Operational Amplifiers for Electromagnetic Susceptibility Analysis

Matteo Vincenzo Quitadamo, *Student Member, IEEE,* Franco Fiori, *Member, IEEE*

***Abstract*—This paper proposes a macromodel to predict the nonlinear behavior of operational amplifiers having their baseband signal affected by out-of-band disturbances, such as those caused by electromagnetic interference (EMI). Like any opamp macromodel, the one proposed in this work was developed with the purpose of not sharing neither the technology parameters nor the circuit topology of the real device. Besides the baseband macromodel, the proposed solution comprises of a high frequency equivalent circuit that propagates the out-of-band signals, and a nonlinear model to account for their demodulation. The proposed solution is suitable for any SPICE-like simulator. It does not affect the simulation performance, meaning the simulation time, the simulation accuracy and it does not cause any convergence issue. This paper shows in detail the macromodel, the method to calculate its parameters as well as its experimental validation, which was obtained comparing the model predictions with the results of the measurements carried out on a commercial device.**

***Index Terms*—Operational Amplifier, Electromagnetic Susceptibility, Macromodel, Nonlinear Model, EMI demodulation, Electromagnetic Interference.**

I. Introduction

Over the years, computer aided analysis has become one of the key steps in the design flow of electronic circuits, as a means to check their compliance to the design specifications as well as their behavior in unexpected conditions such as in the presence of out-of-band interference. This is likely to happen if a circuit comprising an operational amplifier (opamp) is affected by the electromagnetic fields radiated by intended antennas, like those used in wireless communications, or by unintended ones, such as the interconnects of high-speed data link or power switching circuits.

As is known, simulation results are as good as the models used to represent the circuit components [1], therefore, over the years researchers and practitioners have developed new models to obtain higher accuracy levels. This has led to more complex models, which require a greater computational effort resulting in longer simulation times and a higher probability of having simulation convergence issues [2]–[6]. Furthermore, to perform transistor level simulations, the circuit topology and the transistor models, i.e., the technology parameters should be disclosed to the end user, and that is not acceptable by the Intellectual Property (IP) owners. Based on this, simplified linear and nonlinear equivalent circuits including mathematical functions compatible with circuit simulators have been developed to predict the baseband operation of real devices. Regarding opamps, the first macromodel was introduced by Boyle in 1976 [7]. He proposed an equivalent circuit for a BJT opamp. The solution he developed comprises of passive and active elements such as resistors, transistors and diodes, and of behavioural elements, i.e., controlled sources. He showed that simulations performed with such a model are faster, but less accurate than those obtained from the analysis based on transistor level circuits. In [8], the macromodel proposed by Boyle was extended for a CMOS opamp, showing similar properties in terms of circuit complexity and performance. Over time, some authors have improved the Boyle macromodel by including additional features as in [9], others developed new circuit topologies as in [10]–[15] showing the pros and cons of their circuits depending on the features they wanted to better predict. Since such models were developed for predicting the in-band operation, the results they provide are reliable as far as in band signals are concerned, but not with out-of-band signals. Indeed, previous works have shown that real opamps not only propagate high frequency signals like Radio Frequency Interference (RFI), but they demodulate the disturbances superimposed onto the baseband nominal signals [16]–[22]. In [23] it is shown that the demodulation takes mostly place in the opamp input stage, therefore, over the years, researchers an practitioners have developed new input stage topologies aimed to improve the immunity to EMI [24]–[28], [30], [32], but also simulation oriented macromodels for predicting the demodulated EMI [29], [31], [33], [34]. Since the demodulation of the interference takes place in the input stage, some authors explored the possibility of predicting such effects referring to the Boyle macromodel, which include a differential transistor pair as input stage. However, such solutions require the knowledge of design and technology parameters, which are usually not disclosable to end users. Furthermore, the prediction of such models reasonably matches with the experimental results up to $100\,\mathrm{MHz}$ [33], [34]. Besides the macromodels based on Boyle's, some authors developed macromodels with a linear circuits as input stage [12], [13]. These are not suitable for predicting the nonlinear distortion effect by definition. In [29] and in [31], the authors propose macromodels specific for the opamps' susceptibility analysis, without taking into account their base band limitations.

This paper proposes a macromodel that allows one to predict both the in-band and the out-of-band operation of real opamps. As any baseband macromodel, it allows the silicon makers not to share neither the circuit topology nor the technology parameters. Furthermore, it lends itself well to be used with common baseband opamp macromodels, thus it is suitable for any circuit simulator.

The authors are with the Department of Electronics and Telecommunication, Politecnico di Torino, Turin 10129, Italy. (e-mail: matteo.quitadamo@polito.it, franco.fiori@polito.it)

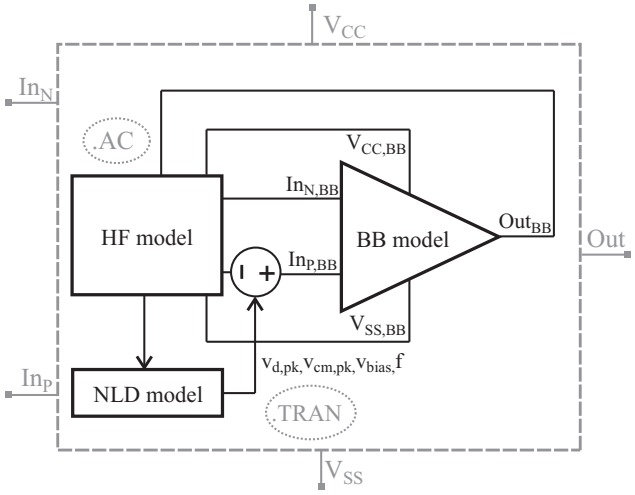

Fig. 1. Architecture of the proposed macromodel.

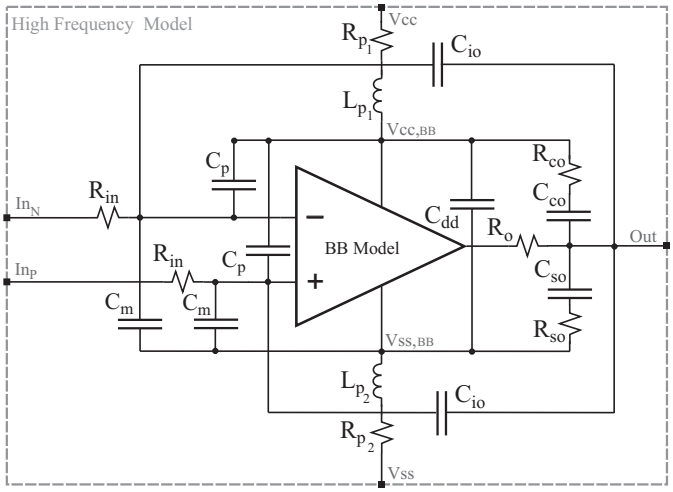

Fig. 2. Proposed high frequency network.

The paper is organized as follows. Section II shows the blocks the macromodel is made of, describes how to extract it and how to evaluate its parameters. Section III shows an experimental verification of the proposed macromodel, comparing its predictions with the results obtained from measurements carried out on a properly configured opamp. Finally, Section IV draws some concluding remarks.

II. OpAmp Susceptibility Model

Wanting to develop a macromodel capable of predicting both the baseband and the out-of-band operation of real opamps, the baseband macromodel (BB model) was complemented with a high frequency model (HF model) of the device and with a nonlinear distortion model (NLD model), as highlighted in the block diagram shown in Fig. 1. Besides the nominal function of the device, the BB model comprises of several non idealities such as the opamp bandwidth, the technology input offset voltage and current, the Slew Rate (SR) limitation and many other parameters, which are not mentioned here for brevity. The HF block includes an equivalent circuit, which propagates out-of-band signals throughout the device. Such circuit includes mainly passive components, i.e., resistances, capacitances and inductances, with the purpose of modelling the parasitic behavior of the integrated circuit and its package. Its presence should not affect the operation of the BB model up to the opamp transition frequency (f_{T}). The third block in Fig. 1, i.e., the NLD model, includes the mathematical functions proposed in [23] to calculate the demodulated interference. Such a model relies on a set of variables resulting from the small signal analysis of the HF model. The proposed model operates in two steps as presented in [35]. At first, the small signal analysis (.AC simulation) of the circuit comprising the proposed model is carried out with the purpose of evaluating the magnitude and the phase of the out of band signals affecting the circuit, thus the variables needed to calculate the demodulated interference are provided to the NLD block of the model. As a second step, the demodulated interference is obtained from time domain analysis (.TRAN simulation) of the circuit including the complete model, which comprises both the HF model and the NLD model. Compared with the analysis of the same circuit at the transistor level, this approach reduces the simulation time significantly because the number of elements included in the macromodel is much lower and because the circuit is driven by baseband signal sources only since the demodulated interference is modeled by an equivalent dc input voltage source.

A. High Frequency Model

As mentioned above, the predictions resulting from the analysis of circuits including opamp baseband models, which are driven by out of band interference, in general do not match neither with those resulting from transistor level simulations nor from experimental results. Aiming to address this issue, the high frequency network shown in Fig. 2, was introduced. This model propagates the out-of-band signals and it does not affect the operation of the BB one. Given that common macromodels works properly up to ten times the opamp transition frequency, the HF model presented hereinafter was developed in order to be effective from that frequency up to 1 GHz.

It is comprised of passive elements only. The input capacitances C_{m} model the capacitive coupling between the inputs and the power supply terminals ($V_{\mathrm{SS,BB}}$) and, as the resistances R_{in}, they represent the ESD protections circuits. The two capacitances C_{p} model the parasitic coupling of the inputs with the positive power supply $V_{\mathrm{CC,BB}}$, while the two pairs of resistances and inductances, $R_{\mathrm{p_1}}$, $R_{\mathrm{p_2}}$ and $L_{\mathrm{p_1}}$, $L_{\mathrm{p_2}}$ connected in series to the positive and to the negative power pins of the BB model represent the package interconnects including the bonding wires. The resistance R_{o} models the high frequency output resistance, which depends on the frequency of the voltage across it. The capacitance C_{so} and the resistance R_{so} model the parasitic coupling of the output terminal to ground at the chip level ($V_{\mathrm{SS,BB}}$). The coupling between the positive power supply node and the output terminal is modelled by the capacitance C_{po} and the resistance R_{po}. The two capacitances C_{io} models the direct coupling of the input pins with the output terminal. All such parasitic elements can be evaluated

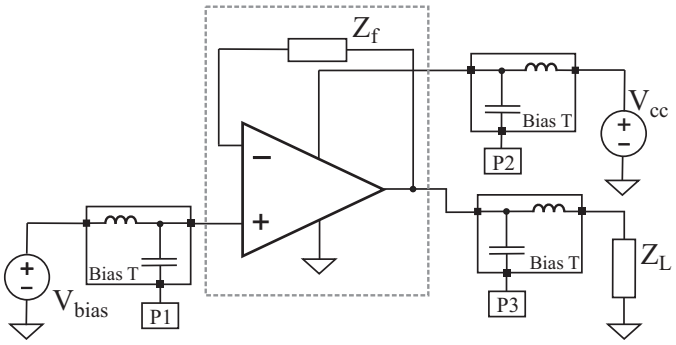

Fig. 3. OpAmp configuration used to extract the scattering parameters of the feedback OpAmp.

exploiting a small signal characterization of the Device Under Test (DUT). More precisely, three scattering matrices (S-par) of the DUT connected in the voltage follower configuration, as shown in Fig. 3, should be obtained from measurements on a real device, or from simulations (small signal analysis) of the circuit at transistor level [42]. However, given that neither the circuit topology of the opamp nor the transistor models are usually disclosed to the end user, the reminder of the paper focuses on scattering parameters obtained experimentally, and on the method used for their measurement. In particular, the test circuit comprises a feedback resistance $\mathrm{R_f}$ of constant value ranging from $1\,\mathrm{k\Omega}$ to $10\,\mathrm{k\Omega}$ that avoids the out-of-band signal to propagate from the input to the output (or vice versa) but it closes the loop for the baseband signals. The DUT shows three ports: the non-inverting input (P1), the positive power supply (P2), and the output terminal (P3), as shown in Fig. 3. Wanting to obtain the S-par matrices experimentally, the test circuit have to include the bias tees at the three ports, P1, P2 and P3. In particular, P1 is needed to supply the DUT and P2 to bias the input port properly. The characterization in terms of scattering parameters of the DUT is performed considering three independent matrices, because they are extracted using a 2-port Vector Network Analyser (VNA), without loading the third port with the reference impedance (Z_{ref}). This was considered during the circuit analysis presented hereinafter, which is aimed to obtain the parameters of the high frequency equivalent circuit shown in Fig. 2. The obtained S-pars are de-embedded [36] to reduce the parasitic effects of the Printed Circuit Board (PCB), and to consider only the parasitic elements related to the integrated circuit. Then, such parameters are converted into the admittance one (Y-pars) by means of (1) and made equal to the ones derived analytically on the basis of the HF model shown in Fig 2.

$$
\begin{aligned}
Y_{\mathrm{ii}} &= \frac{(1-S_{\mathrm{ii}})(1+S_{\mathrm{jj}})+S_{\mathrm{ij}}S_{\mathrm{ji}}}{(1+S_{\mathrm{ii}})(1-S_{\mathrm{jj}})-S_{\mathrm{ij}}S_{\mathrm{ji}}}Y_0, \qquad (1)\\
Y_{\mathrm{ij}} &= -\frac{2S_{\mathrm{ij}}}{(1+S_{\mathrm{ii}})(1-S_{\mathrm{jj}})-S_{\mathrm{ij}}S_{\mathrm{ji}}}Y_0,\\
Y_{\mathrm{ji}} &= -\frac{2S_{\mathrm{ji}}}{(1+S_{\mathrm{ii}})(1-S_{\mathrm{jj}})-S_{\mathrm{ij}}S_{\mathrm{ji}}}Y_0,\\
Y_{\mathrm{jj}} &= \frac{(1+S_{\mathrm{ii}})(1-S_{\mathrm{jj}})+S_{\mathrm{ij}}S_{\mathrm{ji}}}{(1+S_{\mathrm{ii}})(1-S_{\mathrm{jj}})-S_{\mathrm{ij}}S_{\mathrm{ji}}}Y_0.
\end{aligned}
$$

The six independent equations resulting from the evaluation of the Y-pars are not sufficient to calculate the value of HF model parameters. However, the problem can be addressed using the values of the measured parameters in different frequency ranges, since the role played by some model elements is negligible in some frequency bands while it is dominant in some others. The procedure used for assessing the values of the model components can be summarized as follows. With reference to the measurement results, a frequency range in which the measured admittances are mostly capacitive is identified. The expressions of the circuit admittances are simplified by zeroing the parasitic inductances and resistances of the HF model, thus inverted in order to express the circuit capacitances as a function of the admittances obtaining (2)-(7).

$$C_{\mathrm{co}} \simeq -\frac{\mathrm{Im}(Y_{32})}{s} \qquad (2)$$

$$C_{\mathrm{io}} \simeq -\frac{\mathrm{Im}(Y_{31})}{s} \qquad (3)$$

$$C_{\mathrm{dd}} \simeq \frac{\mathrm{Im}(Y_{12}+Y_{22})}{s} \qquad (4)$$

$$C_{\mathrm{so}} \simeq \frac{\mathrm{Im}(Y_{33}+Y_{31}+Y_{32})}{s} \qquad (5)$$

$$C_{\mathrm{p}} \simeq -\frac{(C_{\mathrm{co}}+C_{\mathrm{io}}+C_{\mathrm{so}})\,\mathrm{Im}(Y_{21})+sC_{\mathrm{co}}C_{\mathrm{io}}}{s(C_{\mathrm{co}}+C_{\mathrm{io}}+C_{\mathrm{o}})} \qquad (6)$$

$$C_{\mathrm{m}} \simeq -\frac{(C_{\mathrm{co}}+C_{\mathrm{io}}+C_{\mathrm{so}})\,\mathrm{Im}(Y_{11}+Y_{21})+sC_{\mathrm{so}}C_{\mathrm{io}}}{s(C_{\mathrm{co}}+C_{\mathrm{io}}+C_{\mathrm{so}})} \qquad (7)$$

The value of the parasitic inductances (L_{p}) can be calculated exploiting the coupling between the ports P1 and P2. Indeed, Y_{21} shows two double zeros, f_{rz}, and two double poles f_{rp}, which depend on L_{p1} and $L_{\mathrm{p\text{-}tot}}$, respectively. Therefore, substituting in (8) and (9) the value of the resonance frequencies obtained from the Y-pars measurements, $L_{\mathrm{p\text{-}tot}}$, L_{p1}, thus that of L_{p2} can be derived as shown in (10).

$$L_{\mathrm{p-tot}} \simeq \frac{1}{4\pi^2(C_{\mathrm{dd}}+2C_{\mathrm{p}})f_{\mathrm{rp}}^2} \qquad (8)$$

$$L_{\mathrm{p1}} \simeq \frac{(C_{\mathrm{m}}+C_{\mathrm{p}})(C_{\mathrm{co}}C_{\mathrm{p}}+C_{\mathrm{so}}C_{\mathrm{p}})}{4\pi^2 f_{\mathrm{rz}}^2 C_{\mathrm{dd}}(C_{\mathrm{m}}^2+C_{\mathrm{p}}^2)(C_{\mathrm{co}}+C_{\mathrm{so}})} \qquad (9)$$

$$L_{\mathrm{p2}} \simeq L_{\mathrm{p-tot}} - L_{\mathrm{p1}} \qquad (10)$$

The resistance R_{o} is a frequency dependent parameter, since the value of the low frequency output resistance of the opamp, should not be affected by the introduction of such a component. Accordingly, R_{o} can be modeled as in (11), exploiting the measured Y_{33} parameter and the value of the opamp bandwidth, which equals f_{T} with the opamp connected as voltage follower. In such a way, at the lower frequencies, the value of the output resistance is the one modeled by the BB circuit, while at the higher frequencies it takes the value resulting from the HF model. The resistances R_{co} and R_{so} depend on the coupling between port P3 with internal nodes $V_{\mathrm{CC,BB}}$ and the $V_{\mathrm{SS,BB}}$, respectively. They also depend on the impedance matrix parameters Z_{32} and Z_{33} and can be evaluated using (12) and (13). The value of the two resistances R_{in} is given by (14), while there is no explicit solution for evaluating R_{p1} and R_{p2}. The value of such components can be numerically derived exploiting that taken by Y_{21} at the resonant frequencies f_{rz} and f_{rp}.

$$R_{\rm o} \simeq \frac{s\,\mathrm{Re}((Y_{33}-sC_{\rm o})^{-1})}{s+2\pi f_{\rm BW}} \quad (11)$$

$$R_{\rm co} \simeq \mathrm{Re}\left(\frac{1}{sC_{\rm co}}-Z_{32}\right) \quad (12)$$

$$R_{\rm so} \simeq \mathrm{Re}\left(\frac{1}{sC_{\rm so}}-Z_{33}\right) \quad (13)$$

$$R_{\rm in} \simeq \mathrm{Re}\left(Z_{11}-\frac{1}{s(C_{\rm m}+C_{\rm p})}\right) \quad (14)$$

B. Nonlinear Demodulation Model

As far as common opamps are concerned, it has been shown in previous works that an out-of-band signal superimposed onto the nominal input one is demodulated by a feedback opamp as in RF mixers [23]. In particular, a CW interference affecting the input induces a dc offset at the output ($V_{\rm out}$ in Fig. 4) of magnitude that depends on the interference frequency and magnitude. Furthermore, given that such offset voltage is usually dominated by the RFI rectification in the opamp input stage [37], it has been shown that such an offset can be positive or negative depending on the input stage topology. NMOS differential input stages show negative offset voltage, PMOS input stages show positive offset while rail-to-rail input stages, which combine both NMOS and PMOS differential input stages show offset voltage of sign that depends on the common mode input bias voltage [38]. Wanting to include such a nonlinear effect in the opamp macromodel, a baseband voltage source representing the demodulated interference was connected in series to the non inverting input as shown in Fig. 1 (NLD model). Its magnitude can be expressed as

$$v_{\rm off-inp} = \frac{g_{\rm p}|Y(j\omega)|}{2g_{\rm m}} \cdot B \cdot v_{\rm d,pk} v_{\rm cm,pk}. \quad (15)$$

where

$$B = \cos(\angle Y(j\omega))\cos(\phi_{cm}) - \sin(\angle Y(j\omega))\sin(\phi_{cm}). \quad (16)$$

Equation (15) relates the equivalent input offset voltage of a differential input stage, $v_{\rm off-inp}$, to the peak value ($v_{\rm d,pk}$) of the differential input voltage

$$v_{\rm d} = v^+ - v^-, \quad (17)$$

the peak value ($v_{\rm cm,pk}$) of the common mode input voltage, which is defined as

$$v_{\rm cm} = \frac{v^+ + v^-}{2} \quad (18)$$

and to $\phi_{\rm cm}$, i.e., the phase difference between $v_{\rm d}$ and $v_{\rm cm}$. The other terms in (15), meaning the input stage transconductance $g_{\rm m}$, the demodulation coefficient $g_{\rm p}$ and the parasitic admittance loading the tail of the differential pair $Y(j\omega)$ deal with the specific circuit topology of the input stage and on the semiconductor technology used to design and fabricate it. Given that neither the circuit topology nor the technology parameters can be disclosed with the end users, such a model is not suitable to be included in the macromodel in the present form. Furthermore, it works well under the assumption of weak distortion, which depends on the input signal magnitude. Based on that, (15) can be rewritten as

$$V_{\rm DC,RF} = K(\cos(\phi_{\rm cm}) - \tan(\angle Y)\sin(\phi_{\rm cm})) \cdot v_{\rm d,pk} v_{\rm cm,pk}. \quad (19)$$

where K is the opamp demodulation coefficient. It depends on $v_{\rm d,pk}$, $v_{\rm cm,pk}$, on the frequency of the injected disturbance f and on the input voltage $V_{\rm bias}$ which biases the opamp.

The use of (19) requires to evaluate two parameters: the coefficient K and the phase of $Y(j\omega)$. These can be obtained by imposing $\phi_{\rm cm} = 0$ and exploiting the different sets of offset measurements as a frequency function.

1) Demodulation coefficient K: In order to derive K as a function of the above mentioned parameters for an off-the-shelf opamp, a sample should be inserted in a test setup like that shown in Fig. 4 [39], [40]. Besides the device under test, which is configured as a voltage follower, the circuit comprises of an RF source (an RF Arbitrary Waveform Generator (AWG) cascaded with an RF amplifier), along with a bias tee to provide the opamp with the input nominal signal ($V_{\rm bias}$), a two channel power meter and a directional coupler to measure the incident and reflected power. A dc voltmeter is used to measure the dc output voltage ($V_{\rm out}$) with and without the interference superimposed onto the nominal input voltage, in order to obtain the opamp output offset voltage. As far as such a test setup is concerned and the interference frequency is well above the feedback opamp cut off frequency [23], $v_{\rm cm}$ is about $\frac{v_{\rm d}}{2}$, therefore $v_{\rm d}$ is about that at the non-inverting input to ground (v_+). Based on the above, K can be expressed as

$$K(V_{d,pk}, V_{cm,pk}, f, V_{\rm bias}) = \frac{2V_{off}}{V^2_{+,pk}}, \quad (20)$$

and this can be used to obtain the functions relating K to the input variables, i.e., the peak value of the RF voltage applied to the inputs ($V_{+,pk}$), its frequency (f) and the nominal input voltage ($V_{\rm bias}$). In practice, the experimental characterization of the feedback opamp is performed with the purpose of acquiring the output offset voltage while sweeping one variable at time. Further details about the test bench and the measurement procedure are provided in Section III.

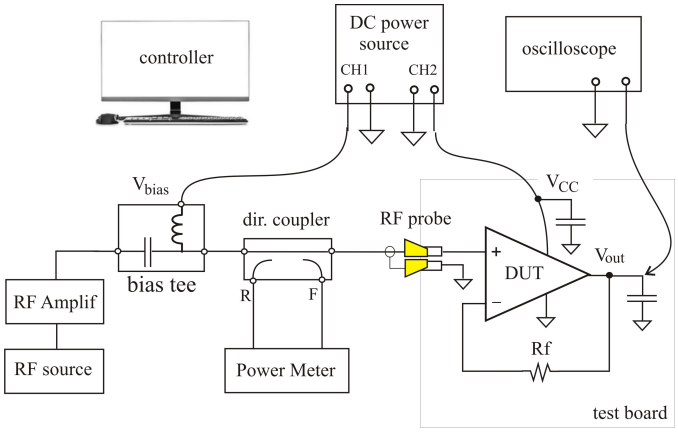

Fig. 4. Test bench for the measurement of the output offset voltage ($V_{\rm off}$).

2) Evaluation of $\angle Y(j\omega)$: This angle can be evaluated exploiting (21) as introduced in [23] for the nMOS differential stage.

$$Y(j\omega) = \frac{j\omega 2g_{\mathrm{m}}C_{\mathrm{T}}}{2g_{\mathrm{m}} + j\omega(2C_{\mathrm{gs}} + C_{\mathrm{T}})} = \frac{C_{\mathrm{T}}(\omega^2/\omega_0) + j\omega C_{\mathrm{T}}}{1 + (\omega/\omega_0)^2} \tag{21}$$

with

$$\omega_0 = \frac{2g_{\mathrm{m}}}{C_{\mathrm{T}} + 2C_{\mathrm{gs}}}. \tag{22}$$

C_{T} is the differential stage tail capacitance, C_{gs} is the gate source capacitance of the differential pair transistors.
Equation (21) allows one to calculate $\angle Y(j\omega)$ as:

$$\angle Y(j\omega) = \mathrm{atan}\Big(\frac{\omega_0}{\omega}\Big). \tag{23}$$

Thus, considering $\angle\phi_{\mathrm{cm}} = 0$:

$$V_{\mathrm{DC,RF}} = \frac{g_{\mathrm{p}}C_{\mathrm{T}}}{2g_{\mathrm{m}}} \frac{(\omega^2/\omega_0)}{1 + (\omega/\omega_0)^2} v_{\mathrm{d,pk}} v_{\mathrm{cm,pk}} = K \cdot v_{\mathrm{d,pk}} v_{\mathrm{cm,pk}} \tag{24}$$

So, considering $\omega >> \omega_0$:

$$K_{\mathrm{high}} \simeq \frac{g_{\mathrm{p}}C_{\mathrm{T}}}{2g_{\mathrm{m}}} \cdot \omega_0 = A \cdot \omega_0. \tag{25}$$

while, for $\omega << \omega_0$:

$$K_{\mathrm{low}} \simeq \frac{g_{\mathrm{p}}C_{\mathrm{T}}}{2g_{\mathrm{m}}} \cdot \frac{\omega^2}{\omega_0} = A \cdot \frac{\omega^2}{\omega_0} \tag{26}$$

The coefficients K_{high} is proportional to ω_0, while K_{low} depends both on ω_0 and ω. This allows one to write two independent equations aimed to obtain ω_0 from the dc offset measured at different frequencies. Therefore, at high frequency, it results

$$\beta_{\mathrm{high}} = K_{\mathrm{high}} = A \cdot \omega_0 \tag{27}$$

while, at lower frequencies:

$$\beta_{\mathrm{low}} = \frac{K_{\mathrm{low}}}{\omega^2} = \frac{A}{\omega_0}. \tag{28}$$

By (27) and (28), it can be found that

$$\omega_0 = \sqrt{\frac{\beta_{\mathrm{high}}}{\beta_{\mathrm{low}}}} \tag{29}$$

therefore $\angle Y(j\omega)$ can be obtained from (23).

3) The Lagrange polynomial fitting: With the aim to obtain a set of functions that relate the K parameter to the input variables, a fitting technique was applied to the multidimensional matrix of the extrapolated data. In this work, the Lagrange fitting technique is adopted [41]. For a given set of data points $(x_i, x_j, \ldots, x_k, z)$, this approach allows one to obtain the lowest degree polynomial, which assumes for each combination of data $(x_i, x_j, \ldots, x_k)$ the value z. The Lagrange polynomial for a multidimensional data array, is defined as follows

$$L(x_i, x_j, \ldots, x_k) = \sum_{k=1}^{M} \ldots \sum_{n=1}^{N} z_n l(x_i) l(x_j) \ldots l(x_k), \tag{30}$$

where N and M are the total number of points that compose the interpolation grid for each variables, and the generic $l(x)$ is one base of the Lagrange polynomial obtained using

$$l_j(x) = \prod_{1<m<k, m\neq j} \frac{x - x_m}{x_j - x_m}. \tag{31}$$

The Lagrange interpolation method has the advantage to generate the exact output value for the points included in the interpolation grid, but for a large number of values, such technique is susceptible to the Runge's phenomenon, resulting in a polynomial with large oscillations. In order to avoid such issue, the interpolation was performed inside the simulation environment, considering polynomials with a maximum degree of two.

4) How to use the Macromodel: Once the NLD model and the HF model have been extracted, they are included in a SPICE netlist like that shown in the Appendix. The analysis of a circuit comprising the proposed macromodel (that shown in Fig. 1) consists of two steps. At first, a small signal analysis (.AC) of the complete circuit should be carried out with the purpose of evaluating the magnitude and phase of the common mode (v_{cm}) and the differential mode (v_{d}) interference due to the external source. These variables are necessary to evaluate K, thus the RFI-induced equivalent input offset voltage. Therefore, the output of the AC analysis along with the frequency of the primary source of interference are used to generate a new netlist including K, which is suitable to perform large signal analysis, meaning .OP or .TRAN analysis [35]. Aiming to avoid doing such a double step by hand, a PowerShell script running in parallel with *LTSpice* [42] was developed. Such a script checks whether the command .EMI, which has been defined in this work for that purpose, is included in the circuit netlist. In such a case, it generates a copy of the original netlist including the .AC simulation command and once the simulation outputs are available it composes a new netlist including the magnitude and phase of v_{d} and v_{cm} and it runs a transient analysis.

III. Experimental Results and Model Validation

In order to apply the proposed method and to check it experimentally, the TS912 opamp was considered [43]. It is an off-the-shelf component featuring rail to rail inputs and output and transition frequency $f_{\mathrm{T}} \simeq 1\ MHz$. A sample of this opamp was included in the test setup shown in Fig. 4, which provided the opamp with 3 V power supply. The input terminal was biased by means of a 1 V dc voltage source, and the S-par matrices 1-2, 1-3 and 2-3 were measured in the frequency range 10 MHz - 1 GHz using a VNA [44]. The port not connected to the VNA was left open as mentioned in Section II A. In order to obtain the HF model parameters, the opamp admittances were evaluated from the S-parameters using (1) then the capacitances were calculated using (2)-(7). Finally the package parasitic inductances and the device equivalent resistances were calculated with (8)-(14). The approximations used to evaluate such parameters are summarized in Table I and the model parameters are listed in Table II. Furthermore, Fig. 6 shows the magnitude and the phase of the Y parameters

TABLE I
FREQUENCY RANGE AND APPROXIMATION USED TO OBTAIN THE HF MODEL PARAMETERS

parameter	Input data	Frequency range/value	circuit semplification
C_m C_p C_{co} C_{io} C_{dd} C_{so}	Y_{12}, Y_{13}, Y_{23}	$50MHz$	L_{xy} and R_{xy} shorted
L_{p1} L_{p2}	Y_{12}	$f_{rz} = 295MHz$, $f_{rp} = 218MHz$	R_{xy} shorted
R_o	Y_{33}	from $10MHz$ to $1GHz$	R_{co} R_{so} R_{in} R_{p1} R_{p2} shorted
R_{co} R_{so} R_{p1} R_{p2} R_{in}	Z_{32}, Z_{33} Y_{12} Z_{11}	from $500MHz$ to $1GHz$ $f_{rz} = 295MHz$, $f_{rp} = 218MHz$ from $100MHz$ to $1GHz$	R_{p1}, R_{p2} R_{in} shorted R_{in} shorted -

TABLE II
VALUES OF THE HIGH FREQUENCY NETWORK COMPONENTS.

Capacitance [pF]		Inductance [nH]		Resistance [Ω]	
C_m	1.63			R_{in}	41
C_p	1.97	L_{p1}	6.11	R_{p1}	2.74
C_{co}	11.23			R_{co}	20.68
C_{io}	0.558			R_o	1.2
C_{dd}	52.87	L_{p2}	3.2	R_{p2}	1.56
C_{so}	1.03			R_{so}	1

Y_{21} and Y_{22} obtained from the measured scattering parameters (dashed lines) and from the AC analysis of the macromodel (continuous line). The simulation results obtained with the BB model only (the HF model was removed) are shown on the top (step 0), those obtained from the circuit comprising the BB model and the HF model capacitances (the inductances and the resistors were shorted) are in the middle (step 1) and those obtained with the BB model and the HF model comprising the capacitances and the inductances are shown on the buttom (step 2). Finally, the Y parameters resulted from the AC analysis of the macromodel comprising the BB model and the complete HF model are compared with those obtained from the measured scattering parameters in Fig. 7. Once the HF model was completed, the test setup was arranged as in Fig. 4 in order to collect the information needed to build up the NLD model. The DUT was mounted on a test board and connected to a two channel dc voltage source, which provided it with the dc power supply $V_{\rm PS}$, and the nominal input voltage $V_{\rm bias}$. The opamp is configured as voltage follower and a resistor ($R_{\rm f} = 1k\Omega$) is included in the feedback to avoid the interference propagated through the amplifier to be fed back to the input. The RF input signal is generated by an RF signal generator cascaded with an RF power amplifier. The RF signal is superimposed onto the dc input voltage with a bias tee and it is applied to the non inverting input by means of an RF probe. The incident and the reflected power are measured with a two-channel power meter connected to a directional coupler. A preliminary calibration at the RF injection point was carried out in order to consider the attenuation due to the directional coupler and the bias tee. Finally the output voltage is measured by a dc voltmeter and all the instruments included in the test bench are controlled by a personal computer (PC). A picture of the test bench is shown in Fig. 5. In particular, the output offset voltage induced by the RFI was measured for $V_{\rm bias}$ ranging from 500 mV to 3 V with 500 mV step, while the interference frequency and magnitude ($V_{\rm p}$) were swept from 10 MHz to 1 GHz and from 150 mV to 2 V, respectively. The

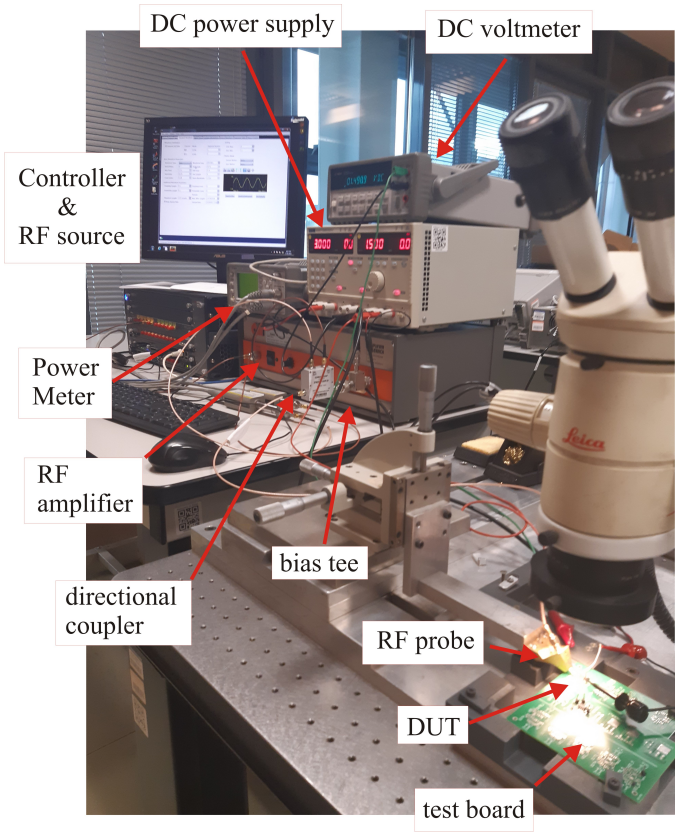

Fig. 5. Picture of the test bench used to measure the offset voltage induced at the opamp output by a CW interference applied at the non inverting input.

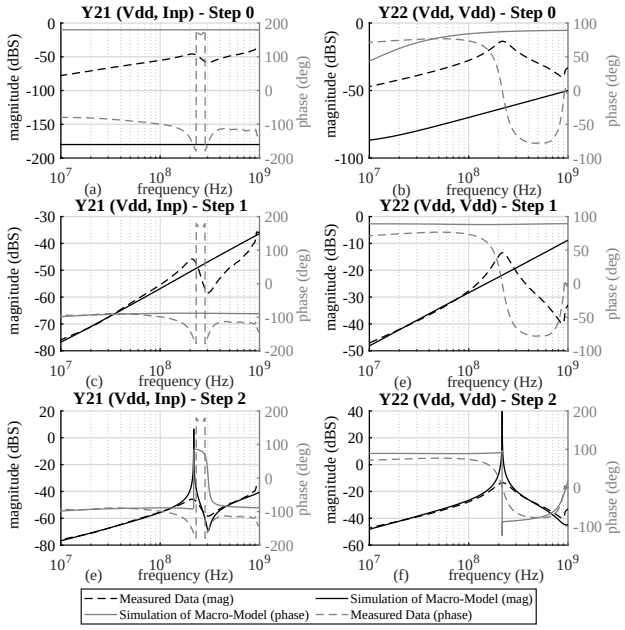

Fig. 6. Comparison of the Y_{21} and Y_{22} admittances (magnitude and phase) obtained from the measured scattering parameters (dashed line) with those resulting from the AC analysis of the macromodel. The parameters resulted from the AC analysis of the BB model without the HF model are shown on the top (step 0), those obtained with the BB model and the HF model capacitances only are in the middle (step 1) and those obtained including the also inductances are on the buttom (step 2).

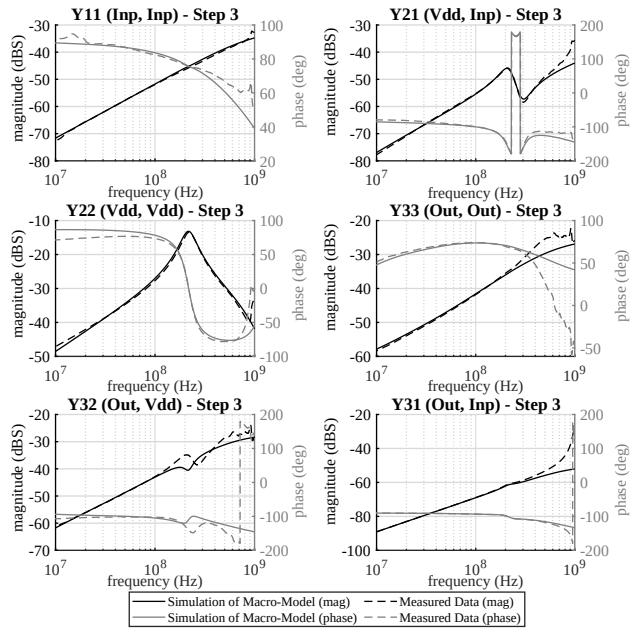

Fig. 7. Comparison of the macromodel admittances (magnitude and phase) obtained from the measured scattering parameters (dashed lines) with those resulting from the AC analysis of the macromodel comprising the BB model and the complete HF model (step 3).

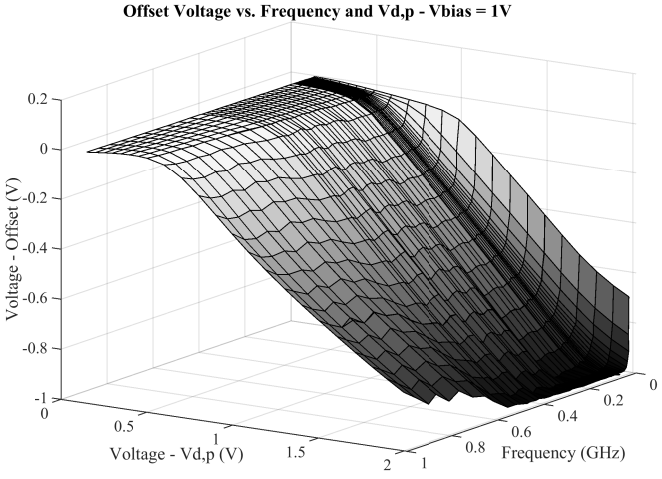

Fig. 8. Offset voltage V_{off} as a function of frequency and $v_{d,p}$ in TS912 with $V_{bias} = 1\,V$.

results obtained for $V_{\rm bias} = 1\,\rm V$ and $V_{\rm bias} = 2.5\,\rm V$ are shown in Fig. 8 and Fig. 9, respectively. They show that the output offset voltage changes its magnitude and sign depending on the input bias level. Indeed, for $V_{\rm bias} = 1\,\rm V$, the offset is negative and increases with the interference magnitude, while for $V_{\rm bias} = 2.5\,\rm V$, it is positive and for RF input voltage ($v_{\rm d,pk}$) above 1 V it falls down to become negative. The results of these offset characterizations are used for evaluating the K coefficient and $\angle Y(j\omega)$. The trend of the K coefficients for $V_{\rm bias} = 1\,\rm V$ is shown in Fig. 10.

With the purpose of validating the model presented so far, the circuit shown in Fig. 11 was considered. It comprises the DUT connected as voltage follower and a second order low pass filter ($L_{\rm e} = 7.8\,\rm nH$ $R_{\rm e} = 3.8\,\Omega$ $C_{\rm e} = 100\,\rm pF$), which

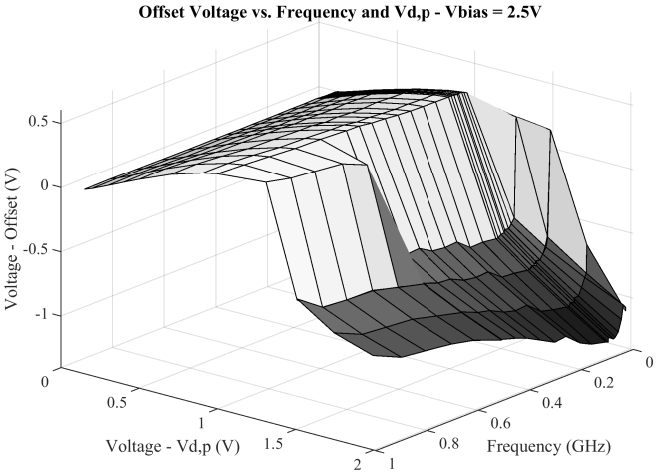

Fig. 9. Offset voltage V_{off} as a function of frequency and $v_{d,p}$ in TS912 with $V_{bias} = = 2.5\,V$.

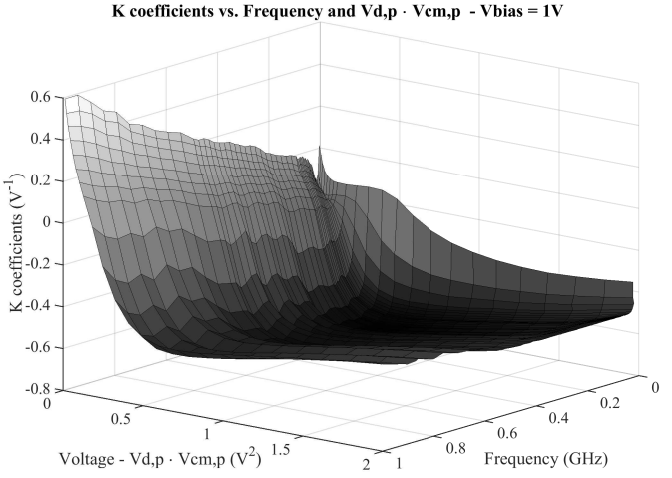

Fig. 10. K coefficients as a function of frequency, $V_{d,p}$ and $V_{cm,p}$ in TS912 with $V_{bias} = 1\,V$.

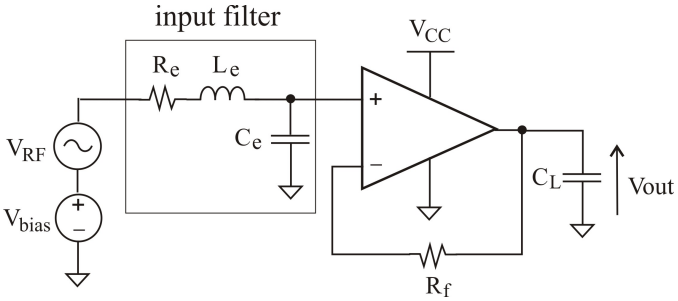

Fig. 11. Test circuit including the RLC input filter connected to the opamp non inverting input.

resonates at 180 MHz. The interference ($V_{\rm RF}$) is superimposed onto the input bias voltage ($V_{\rm bias}$) with a bias tee (not shown in Fig. 11). The susceptibility of such a circuit to the interference was evaluated using the test setup shown is Fig. 4. The offset voltage induced by the RF interference applied at the input was measured. The magnitude of the interference and the input bias voltage were kept constant while sweeping the interference frequency in the range 10

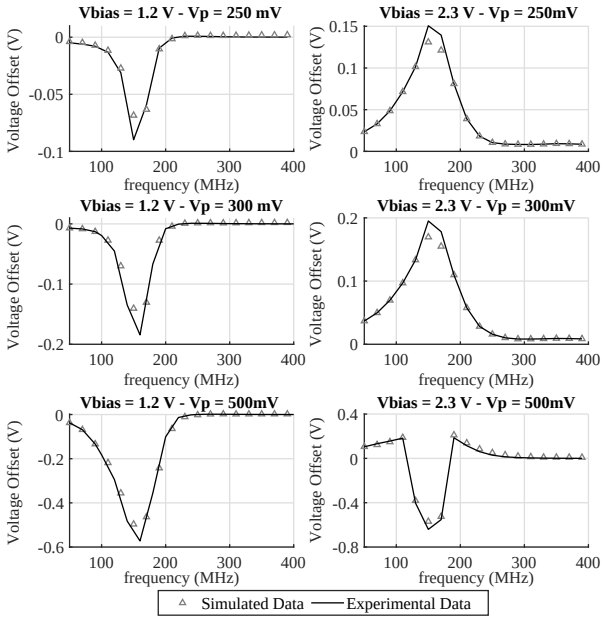

Fig. 12. Comparison between measured (dashed lines) and simulated (triangular dots) results, which were obtained from the time domain analysis of the circuit comprising the proposed macromodel and the RLC input filter.

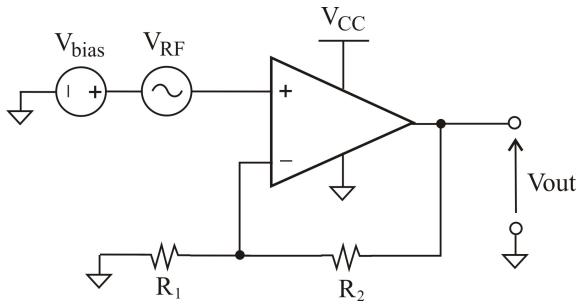

Fig. 13. Test circuit including an opamp based non inverting feedback amplifier.

MHz to 400 MHz where the input filter resonance takes place. These measurements were repeated for different values of the interference magnitude and of the input bias level obtaining the results shown in Fig. 12. The circuit used to perform the experimental tests was replicated in *LTSpice* including the opamp macromodel developed within this work. The comparison of the simulation results with the measurement results is shown in Fig. 12. Later, the feedback resistance R_f was substituted with a short circuit, R_e with a $1.7\,\Omega$ resistor, and the test was repeated using two different values of C_e, $100\,\mathrm{pF}$ and $10\,\mathrm{pF}$, to change the resonant frequency of the input filter and its Q factor and to verify the effectiveness of the model in this conditions. The results of such comparisons, with different bias voltages, are shown in Fig. 15. Further validation was performed considering the test circuit shown in Fig. 13.

Further validation was performed considering the test circuit shown in Fig. 13. The opamp was configured to set the voltage gain to 2 ($R_1 = R_2 = 2\,\mathrm{k}\Omega$). The comparison between the offset voltage resulting from measurements and that obtained

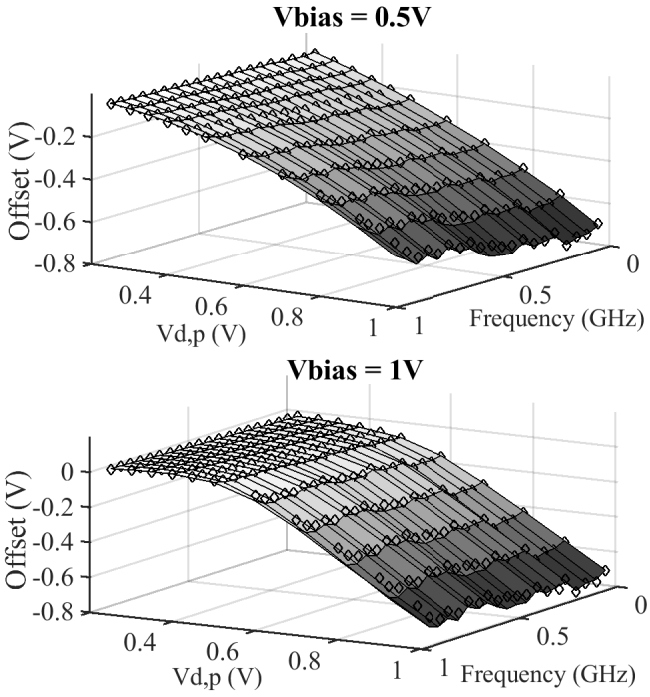

Fig. 14. Comparison between the measured (continuous) and macromodel predicted (diamond dots) output offset voltage of the TS912 connected as in Fig. 13 with voltage gain $A_v = 2$. Two different input bias voltage are considered.

from simulations is shown in Fig. 14, for two different input bias voltages. Also in this case, the simulation results are in good agreement with the experimental ones.

IV. Conclusion

In this work a macromodel suitable for predicting the operation of feedback operational amplifiers in the presence of out of band signals has been proposed. Besides the base-band model, it includes a high frequency equivalent circuit and a nonlinear distortion model, which predict the demodulation of out of band signals carried out by the opamp.

The paper proposes a method for deriving the high frequency equivalent network of an opamp starting from its scattering parameters matrix and a method for modeling its nonlinear behavior when its base-band signals are affected by radio frequency interference. To this purpose, the nonlinear behavior was modeled referring to the Lagrange polynomial interpolation technique. The proposed macromodel can be complemented to any opamp BB model, like those commonly provided by opamp manufacturers, without affecting neither the simulation performance nor the operation of the original BB model. Furthermore, the proposed approach is suitable to be used in any simulation environment providing accurate predictions of both the propagated and demodulated interference, regardless of the circuit configuration, and the PCB parasitic elements.

Appendix

The structure of an LTSpice compatible netlist of the proposed macromodel is reported and commented in this

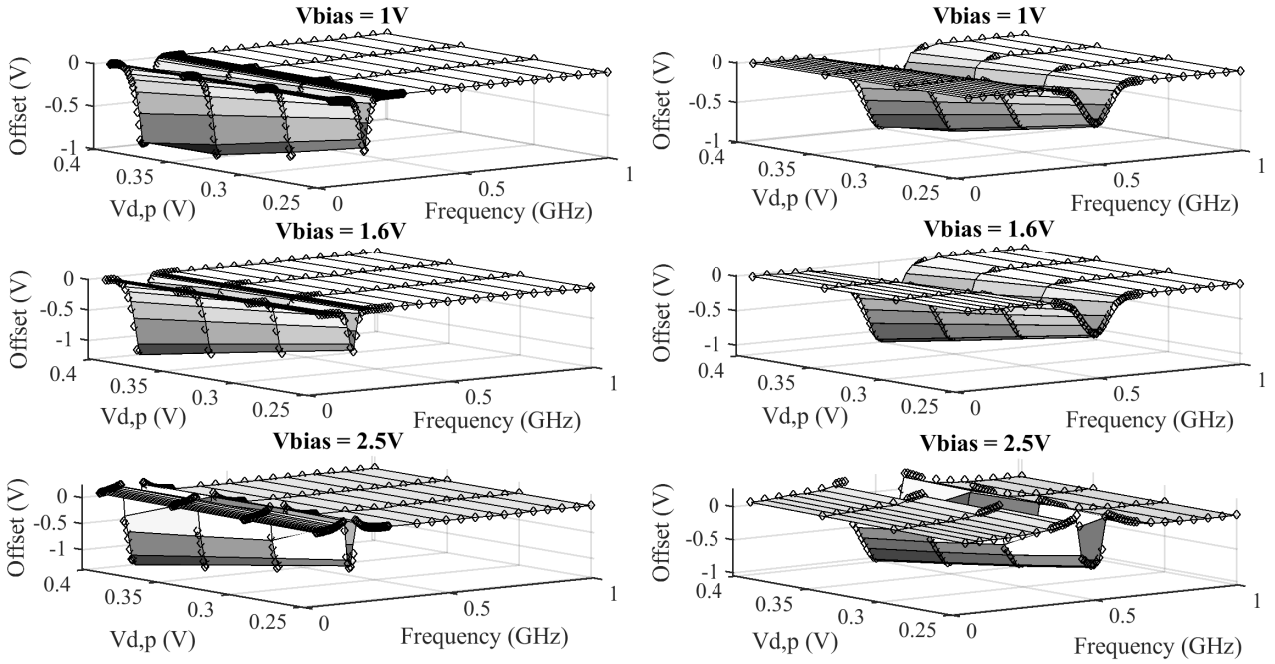

Fig. 15. Comparison of the measured (continuous) and macromodel predicted (diamond dots) output offset voltage of the TS912 opamp included in the circuit shown in Fig. 11 with $C_e = 100\,pF$ (left plots) and $C_e = 10\,pF$ (right plots) for input bias voltage of $V_{bias} = 1\ V$, $V_{bias} = 1.6\ V$ and $V_{bias} = 2.5\ V$.

appendix.

```
.SUBCKT OPAMP_RF inp inn vcc vss out PARAMS: RF_ON=0
+RF_del=0 RF_B=0 RF_F=0 RF_A=0 PHI_CM=0

B_ON_OFF net_on_off 0 V = if({RF_ON}<0.5,0,1)
B_V1 nB 0 V = if({abs(RF_B)}<B1,B1,
+if({abs(RF_B)}>B2,B2,{abs(RF_B)}))
B_V2 nF 0 V = if({abs(RF_F)}<F1,F1,
+if({abs(RF_F)}>F2,F2,{abs(RF_F)}))
B_V3 nA 0 V = if({abs(RF_A)}<A1,A1,
+if({abs(RF_A)}>A2,A2,{abs(RF_A)}))
```

The previous lines of the netlist introduce the interfacing pins of the OpAmp OPAMP_RF and its input parameters, RF_ON and RF_del, which allow one to activate the demodulation block ant to set the time delay after which the RF injection starts, respectively. The RF_B, RF_F and RF_A parameters are the independent variables of the K coefficient function. More precisely, RF_B represents the input bias of the opamp, RF_F, the frequency of RF disturbance and RF_A the product $v_{d,pk}v_{cm,pk}$. The three behavioural voltage sources B_V1, B_V2 and B_V3 are needed to clamp the value of the input variables to the boundaries of the interpolation test grid.

```
B_IND1 nind_1 0 V = table(V(nB),B1,...B2)
B_IND_INT1 nind_int1 0 V = round(V(nind_1))

B_IND2 nind_2 0 V = table(V(nF),F1,...F2)
B_IND_INT2 nind_int2 0 V = round(V(nind_2))

B_IND3 nind_3 0 V = table(V(nA),A1,...A2)
B_IND_INT2 nind_int3 0 V = round(V(nind_3))

BCORD_B1 nc_B1 0 V = if(V(nind_int1)<=2,1,
+if(V(nind_int1)-2+2>NPB,NPB-1,V(nind_int1)-2+1))
BCORD_B2 nc_B2 0 V = if(V(nind_int1)<=2,2,
+if(V(nind_int1)-2+2>NPB,NPB,V(nind_int1)-2+2))
```

```
B_CORD_F1 nc_F1 0 V = if(V(nind_int2)<=2,1,
+if(V(nind_int2)-2+2>NPF,NPF-1,V(nind_int2)-2+1))
B_CORD_F2 nc_F2 0 V = if(V(nind_int2)<=2,2,+
if(V(nind_int2)-2+2>NPF,NPF,V(nind_int2)-2+2))

B_CORD_A1 nc_A1 0 V = if(V(nind_int3)<=3,1,
+if(V(nind_int3)-2+3>NPA,NPA-2,V(nind_int3)-2+1))
B_CORD_A2 nc_A2 0 V = if(V(nind_int3)<=NPA,2,+
if(V(nind_int3)-2+3>NPA,NPA-1,V(nind_int3)-2+2))
B_CORD_A3 nc_A3 0 V = if(V(ind_int3)<=NPA,3,
+if(V(ind_int3)-2+3>NPA,NPA,V(ind_int3)-2+3))
```

The behavioural voltage sources B_IND1, B_IND2 and B_IND3 detect the closest index of the input variables inside the input test arrays. The output of such sources are used to identify the coordinates (B_CORD) of interpolation cube in which will be calculated and evaluated the moving Lagrange polynomial. In the proposed example are used 2 points for the bias and frequency variables while three points for the amplitude one. The three parameters NPB NPF and NPA are the total number of points for each variables of the interpolation grid.

```
B_B1 n_B1 0 V = table(V(nc_B1),1,B1,...,NPB,B2)
B_B2 n_B2 0 V = table(V(nc_B2),1,B1,...,NPB,B2)

B_F1 n_F1 0 V = table(V(nc_F1),1,F1,...,NPF,F2)
B_F2 n_F2 0 V = table(V(nc_F2),1,F1,...,NPF,F2)

B_A1 n_A1 0 V = table(V(nc_A1),1,A1,...,NPA,A2)
B_A2 n_A2 0 V = table(V(nc_A2),1,A1,...,NPA,A2)
B_A3 n_A3 0 V = table(V(nc_A3),1,A1,...,NPA,A2)

B_SEL1 n_sel1 0 V = (V(nc_B1)-1)*NPF*NPA
+ (V(nc_F1)-1)*NPA + V(nc_A1)
B_SEL1 n_sel2 0 V = (V(nc_B2)-1)*NPF*NPA
+ (V(nc_F1)-1)*NPA + V(nc_A1)
.
.
```

```
B_SEL12 n_sel12 0 V = (V(nc_B2)-1)*NPF*NPA
+ (V(nc_F2)-1)*NPA + V(nc_A3)

B_K1 n_k1 0 V = table(V(n_sel1),1,k1,...,
+NPF*NPA*NPB,k_end)
B_K2 n_k2 0 V = table(V(n_sel2),1,k1,...,
+NPF*NPA*NPB,k_end)
.
.
B_K12 n_k2 0 V = table(V(n_sel3),1,k1,...,
+NPF*NPA*NPB,k_end)
B_PH_Y n_p 0 V = table(V(n_ind2),1,PH1,...,
+NPF,PH_end)
```

The output of the B_CORD sources are used to identify some of the input variables of the Lagrange polynomial (B_B B_F and B_A) and to calculate the one-dimensional selectors of the K coefficient for each combinations of the input variables(B_SEL). In the proposed case, 12 selectors are needed to identify 12 values of the evaluated K coefficients (B_K) that will be used for evaluating the offset for the required values of the input variables. The B_PH_Y returns the value of the phase of $\mathrm{Y}(\mathrm{j}\omega)$ as function of the frequency.

```
B_OFF k_coeff 0 V = ((V(n_k1)*({abs(RF_A)} -
+ V(n_A2))*({abs(RF_A)} - V(n_A3))*({abs(RF_B)})...)

B_OUT n_off_lag1 n_off_lag2 V = if(V(net_on_off)<=0,0,
+if(time<{RF_del},0,V(k_coeff)*(cos(PHI_CM)
+ -tan(V(n_p)sin(PHI_CM)){abs(RF_A)}))

X1 n_off_lag1 inn_BB V_CC_BB VSS_BB OUT_BB
OPAMP_BB level.2
X2 n_off_lag2 inn_BB V_CC_BB VSS_BB OUT_BB
+inn_BB V_CC_BB VSS_BB OUT_BB OPAMP_HF
.ENDS
```

The B_OFF source contains the Lagrange polynomial for evaluating the K coefficients, while the B_OUT source returns the $V_{DC,RF}$ offset, exploiting (19). The two instances X1 and X2 are two subcircuits that link the NLD model to the HF and to the BB ones.

REFERENCES

[1] J. Alvin Connelly and Pyung Choi. *Macromodeling with SPICE.* New Jersey: Prentice-Hall Inc., 1992.

[2] C. C. McAndrew et al., "VBIC95, the vertical bipolar inter-company model," *IEEE J. Solid-State Circuits*, vol. 31, no. 10, pp. 1476-1483, Oct. 1996.

[3] H. K. Gummel and H. C. Poon, "An integral charge control model of bipolar transistors," *The Bell System Technical Journal*, vol. 49, no. 5, pp. 827-852, May-June 1970.

[4] C. Pouant, F. Torrès, A. Reineix, P. Hoffmann, J. Raoult and L. Chusseau, "Modeling and Analysis of Large-Signal RFI Effects in MOS Transistors," *IEEE Trans. on Electromagn. Compat.*, vol. 61, no. 1, pp. 111-120, Feb. 2019.

[5] T. Sakurai and A. R. Newton, "A Simple MOSFET Model for Circuit Analysis and its application to CMOS gate delay analysis and series-connected MOSFET Structure", ERL Memo No. ERL M90/19, Electronics Research Laboratory, University of California, Berkeley, March 1990.

[6] Bashir Al-Hashimi. 1995. *The Art of Simulation Using PSpice: Analog and Digital (1st. ed.).* CRC Press, Inc., USA.

[7] G. R. Boyle, D. O. Pederson, B. M. Cohn and J. E. Solomon, "Macromodeling of integrated circuit operational amplifiers," *IEEE J. Solid-State Circuits*, vol. 9, no. 6, pp. 353-364, Dec. 1974.

[8] G. Krajewska and F. E. Holmes, "Macromodeling of FET/bipolar operational amplifiers," *IEEE J. Solid-State Circuits*, vol. 14, no. 6, pp. 1083-1087, Dec. 1979.

[9] C. Turchetti and G. Masetti, "A macromodel for integrated all-MOS operational amplifiers," *IEEE J. Solid-State Circuits*, vol. 18, no. 4, pp. 389-394, Aug. 1983.

[10] P. Weil, L. P. McNamee, "A nonlinear macromodel for operational amplifiers", *Int. J. Circ. Theor. Appl.*, vol. 6, no. 1, pp. 57-64, 1978.

[11] B. Perez-Verdu, J. L. Huertas and A. Rodriguez-Vazquez, "A new nonlinear time-domain op-amp macromodel using threshold functions and digitally controlled network elements," *IEEE J. Solid-State Circuits*, vol. 23, no. 4, pp. 959-971, Aug. 1988.

[12] M. E. Brinson and D. J. Faulkner, "Modular SPICE macromodel for operational amplifiers," *IEE Proc. Circuits, Devices and Systems*, vol. 141, no. 5, pp. 417-420, Oct. 1994.

[13] R. V. Peic, "Simple and accurate nonlinear macromodel for operational amplifiers," *IEEE J. Solid-State Circuits*, vol. 26, no. 6, pp. 896-899, June 1991.

[14] C. Sánchez-López, M. A. Carrasco-Aguilar, F. E. Morales-López, R. Ochoa-Montiel and R. Ilhuicatzi-Roldán, "Spice-compatible nonlinear Op Amp and CFOA macro-models," *Proc. 2014 IEEE Central America and Panama Convention (CONCAPAN XXXIV)*, Panama City, pp. 1-4.

[15] J. H. A. Feijes, R. Hogervorst and J. H. Huijsing, "Macromodelling operational amplifiers," *Proceedings of IEEE Int. Symp. on Circuits and Systems*, London, UK, 1994, vol. 5, pp. 681-684.

[16] Jean-Michel Redouté, Michiel Steyaert, *EMC of Analog Integrated Circuits*, New York: Springer, 2010.

[17] S. Graffi, G. Masetti, A. Piovaccari, "Criteria to reduce failures induced from conveyed electromagnetic interferences on CMOS operational amplifiers", *Microelectron. Reliab.*, Vol. 37, no. 1, pp. 95-113, Jan. 1997.

[18] G. Masetti, S. Graffi, D. Golzio, Z .M. Kovacs, "Failures induced on analog integrated circuits by conveyed electromagnetic interferences: a review", *Microelectron. Reliab.*, vol. 36, no. 7, pp. 955-972, July 1996.

[19] J. G. Tront, J. J. Whalen, C. E. Larson and J. M. Roe, "Computer-Aided Analysis of RFI Effects in Operational Amplifiers," *IEEE Trans. on Electromagn. Compat.*, vol. 21, no. 4, pp. 297-306, Nov. 1979.

[20] F. Fiori, P.S. Crovetti, "Investigation on RFI Effects on Bandgap Voltage References," *Microelectronics Journal*, vol. 35, no. 6, pp. 557-561, June 2004.

[21] F. Fiori, "On the Susceptibility of Chopper Operational Amplifiers to EMI," *IEEE Trans. on Electromagn. Compat.*, vol. 58, no. 4, pp. 1000-1006, Aug. 2016.

[22] F. Fiori, "EMI-Induced Distortion of Baseband Signals in Current Feedback Instrumentation Amplifiers," *IEEE Trans. on Electromagn. Compat.*, vol. 60, no. 3, pp. 605-612, June 2018.

[23] F. Fiori and P. S. Crovetti, "Nonlinear effects of radio-frequency interference in operational amplifiers", *IEEE Trans. on Circuits and Systems I: Fundamental Theory and Applications*, vol. 49, no. 3, pp. 367-372, March 2002.

[24] S. Boyapati, J. Redouté and M. S. Baghini, "Modeling and Design of EMI-Immune OpAmps in 0.18-μm CMOS Technology," *IEEE Trans. on Electromagn. Compat.*, vol. 58, no. 5, pp. 1609-1616, Oct. 2016.

[25] S. Boyapati, J. Redouté and M. S. Baghini, "A robust CMOS miller OpAmp with high EMI-immunity," *Int. Symp. on Electromagnetic Compatibility - EMC Europe*, Angers, FR, 2017, pp. 1-6.

[26] S. Boyapati, J. Redouté and M. S. Baghini, "A highly EMI-immune folded cascode OpAmp in 0.18μm CMOS technology," *Int. Symp. on Electromagnetic Compatibility - EMC Europe*, Wroclaw, PL, 2016, pp. 546-551.

[27] J. Gundla, S. Boyapati and V. S. R. Pasupureddi, "Compact CMOS Miller OpAmp With High EMI-Immunity," *IEEE Trans. on Electromagn. Compat.*, vol. 62, no. 6, pp. 2394-2400, Dec. 2020.

[28] M. Grassi, J. Redouté and A. Richelli, "Increased EMI immunity in CMOS operational amplifiers using an integrated common-mode cancellation circuit," *Int. Symp. on Electromagnetic Compatibility - EMC Europe*, Dresden, D, 2015, pp. 34-39.

[29] J. Gago, J. Balcells, D. GonzÁlez, M. Lamich, J. Mon and A. Santolaria, "EMI Susceptibility Model of Signal Conditioning Circuits Based on Operational Amplifiers," *IEEE Trans. on Electromagn. Compat.*, vol. 49, no. 4, pp. 849-859, Nov. 2007.

[30] D. Zupan and B. Deutschmann, "Comparison of EMI Improved Differential Input Pair Structures Within an Integrated Folded Cascode Operational Transconductance Amplifier," *Austrochip Workshop on Microelectronics*, Wien, Austria, 2020, pp. 47-52.

[31] A. Boyer and E. Sicard, "A Case Study to Apprehend RF Susceptibility of Operational Amplifiers," *12th Int. Workshop on the Electromagnetic Compatibility of Integrated Circuits (EMC Compo)*, Hangzhou, China, 2019, pp. 13-15.

[32] J. Redoute and M. Steyaert, "A CMOS source-buffered differential input stage with high EMI suppression," ESSCIRC 2008, *34th European Solid-State Circuits Conference*, Edinburgh, UK, 2008, pp. 318-321.
[33] G. K. C. Chen and J. J. Whalen, "Using a Macromodel to Predict RFI in Bipolar Operational Amplifiers," *IEEE Int. Symp. on Electromagnetic Compatibility*, Baltimore, USA, 1980, pp. 52-58.
[34] S. Graffi, G. Masetti and D. Golzio, "New macromodels and measurements for the analysis of EMI effects in 741 op-amp circuits," in IEEE Transactions on Electromagnetic Compatibility, vol. 33, no. 1, pp. 25-34, Feb. 1991.
[35] F. Fiori, "Susceptibility of CMOS Voltage Comparators to Radio Frequency Interference," *IEEE Trans. on Electromagn. Compat.*, vol. 54, no. 2, pp. 434-442, Apr. 2012.
[36] Kim, Ju-Young, Choi, Min-Kwon,Lee, Seonghearn, "A "Thru-Short-Open" De-embedding Method for Accurate On-Wafer RF Measurements of Nano-Scale MOSFETs," *Journal of Semiconductor Technology and Science*, vol. 12 no. 1, pp. 53-58, Jan. 2012.
[37] F. Fiori, "A new nonlinear model of EMI-induced distortion phenomena in feedback CMOS operational amplifiers," *IEEE Trans. on Electromagn. Compat.*, vol. 44, no. 4, pp. 495-502, Nov. 2002.
[38] F. Fiori and P. S. Crovetti, "Complementary differential pair with high immunity to RFI," *Electronics Letters*, vol. 38, no. 25, pp. 1663-1664, 5 Dec. 2002.
[39] M. Girard, T. Dubois, G. Duchamp and P. Hoffmann, "EMC susceptibility characterization of an operational amplifier-based circuit combining different technique," *Int. Symp. on Electromagnetic Compatibility - EMC Europe*, Wroclaw, PL, 2016, pp. 300-305.
[40] *Integrated Circuits, Measurement of Electromagnetic Immunity,* 150 kHz-1 GHz, IEC Standard, IEC62132-4, 2006.
[41] A. Quarteroni, F. Saleri, *Scientific Computing with MATLAB. Texts in computational science and engineering,* New York: Springer, 2003.
[42] G. Alonso. (2019, Dec. 10) LTspice User Manual [Online]. Available at http://www.analog.com
[43] TS912 Datasheet [Online]. Available at https://www.st.com
[44] Keysights ENA5080A User Manual [Online]. Available at https://www.keysight.com